Low-Noise Propeller Design with the Vortex Lattice Method and Gradient-Based Optimization

Daniel Ingraham*
NASA Glenn Research Center, Cleveland, Ohio, 44135

This work aims to combine an aerodynamic model based on the unsteady vortex lattice method with an acoustic model provided by Farassat's formulation 1A to perform gradient-based propeller optimizations with aerodynamic and acoustic constraints. Two optimization cases are attempted and successfully converged: an isolated propeller and a propeller-wing configuration, both operating in a 0.11 Mach freestream, representative of a cruise condition. The results show that simultaneously decreasing the RPM and increasing the collective angle of a propeller is an effective noise reduction technique, as expected, and little difference is observed between the two cases. A vortex dissipation model was found to be needed to stabilize the derivatives of the vortex lattice outputs, and a constraint on the propeller blade's chord distribution concavity was needed to produce realistic-looking blade chord distributions.

I. Introduction

Noise, especially rotor or propeller noise, is anticipated to be a critical factor in the design of urban air mobility (UAM) and advanced air mobility (AAM) vehicles. As discussed by Rizzi et al. [1], UAM/AAM vehicle designers need tools that allow them to quickly determine the effect design changes have on vehicle aerodynamic and acoustic performance. Such tools need to be fast and accurate enough to qualitatively capture impacts from these changes, and ideally would be able to determine optimal configurations for a given objective and set of design constraints. Computational fluid dynamics (CFD), while quite general and powerful, is as of yet still too computationally intensive to be used in routine optimizations, especially when acoustic predictions are needed (though there is promising work in this area, e.g., Içke et al. [2]). Lower-order propeller aerodynamic prediction tools like blade element momentum theory (BEMT) work quite well in simplified situations, and can be used for low-noise design (see Ingraham et al. [3]), but are limited in the types of problems they can reasonably attack.

The vortex lattice method (VLM, c.f. [4, 5]) is an attractive approach to predicting aerodynamic forces on lifting surfaces. More capable than pseudo-2D approaches like BEMT, it has considerably more modest computational requirements than CFD. Others have investigated using the vortex lattice method to design optimal propellers. Chang and Sullivan[6] optimized the twist distribution of a propeller blade subject to a shaft power constraint via a VLM implementation and gradient-based optimization. Miller[7] used VLM and gradient-based optimization to show the effect the twist and chord distribution, propeller sweep, diameter, rotation rate, and blade count have on aerodynamic efficiency and noise. Cho and Lee[8] found optimal propeller blade twist and chord distributions, again using gradient-based optimization and a VLM. Finally, Burger et al.[9, 10] combined a VLM implementation and a genetic algorithm to perform single and multi-objective propeller aerodynamic optimizations, and included noise constraints[10].

In this work, we combine an aerodynamic model provided by an unsteady VLM with an acoustic model based on Farassat's formulation 1A [11] to perform gradient-based propeller optimizations with both aerodynamic and acoustic constraints. Unlike all the references cited in the previous paragraph, we will use an unsteady VLM with a "free wake," i.e. the propeller wake's motion will be influenced by the velocity induced by the bound vortices (used to model the propeller blades and other lifting surfaces) and the wake vortices. This combination of an unsteady, free-wake VLM, acoustics model, and gradient-based optimization applied to the problem of propeller design does not exist in the literature to our knowledge.

II. Models and Approach

The code VortexLattice.jl† provides the VLM implementation for this work. In particular, we use the unsteady form of the vortex lattice method that VortexLattice.jl provides, a "free wake" implementation closely following that

*Research Aerospace Engineer, Acoustics Branch, MS 54-3, Member AIAA
†`https://github.com/byuflowlab/VortexLattice.jl`

number of blades	3
propeller diameter	24 inches
hub diameter	4.8 inches
chord	1.5 inches
pitch	16 inches
twist	Helical, see equation 2
design RPM	≈ 7100
airfoil cross-section	NACA 0012

Table 1 Parameters for the baseline propeller design

described in Chapter 13 of Katz and Plotkin [4]. In addition to the free-wake unsteady VLM, VortexLattice.jl also approximates compressibility effects through the usual Prandtl-Glaurert correction

$$F_{\text{comp}} = \frac{F}{\sqrt{1 - M^2}} \tag{1}$$

where F is the incompressible force on the panel surface computed by the VLM and M is the local Mach number. Viscous loading is approximated by calculating a lift coefficient for spanwise stations along the blade, and then using a drag polar to estimate the drag force at the station.

We use the compact form of Farassat's formulation 1A [11] (see also [12]), including the compact monopole approximation of Lopes [13] to calculate the tonal noise produced by the propeller. Farassat's formulation 1A (F1A) is an acoustic analogy, i.e, a rearrangement of the Navier-Stokes equations into a left hand "propagation" and right hand "source" sides. The acoustic analogy equation takes the form of an inhomogeneous wave equation, and is solved using a free-space Green's function. The application of the Green's function to the acoustic analogy equation results in two surface integrals and one volume integral. The two surface integrals represent the noise due to the thickness and loading on the blade's surface, while the volume integral captures nonlinear sources of sound off the surface (e.g., shocks and turbulence). The volume integral is neglected in this work, as the blade tip speeds in the target problem are low. The "compactness" of the approach refers to the simplification of the source's geometry (here, the propeller blade). As discussed by Lopes, if the acoustic source is elongated in one direction and the observer is sufficiently far from the source, the surface integrals associated with the Green's function can be replaced by line integrals along the blade's span. This results in considerable computational cost savings in the acoustic model.

Results are compared to a baseline propeller design [14] throughout this work. Parameters of the baseline design are displayed in Table 1. The propeller twist is defined by

$$\phi(r) = \arctan\left(\frac{P}{\pi D \frac{r}{R}}\right), \tag{2}$$

where r is the radial location along the blade's span, D and P are the diameter and pitch defined in Table 1, and R is the propeller tip radius. The propeller blade was discretized with 20 and 6 panels in the spanwise and chordwise directions, respectively.

We compare the VortexLattice.jl thrust and torque coefficient predictions for the baseline propeller design (Table 1) to experimental data from NASA Langley's Low Speed Acoustic Wind Tunnel (LSAWT) facility in Figure 1. We see that that thrust coefficient agrees well with the experimental data, especially for the higher advance ratios. The torque coefficient is slightly underpredicted throughout the entire range of advance ratios. VortexLattice.jl relies on drag coefficient polars to predict viscous loading, which makes up the majority of the loading in the circumferential direction, responsible for the torque. Adjustment of these polars may improve agreement with the experimental data, but overall we feel the accuracy of the predictions is adequate for the preliminary design workflow this work aims to develop.

We compare acoustic predictions for the VortexLattice.jl+AcousticAnalogies.jl toolchain to LSAWT data for the baseline propeller design at an advance ratio of 0.523 in Figure 2. The sound pressure level (SPL) for the blade passing frequency (BPF) and two and three BPF are shown along the abscissa, from left to right. The polar angle indicates the microphone position, with angles less than 90° corresponding to positions upstream of the propeller, greater than

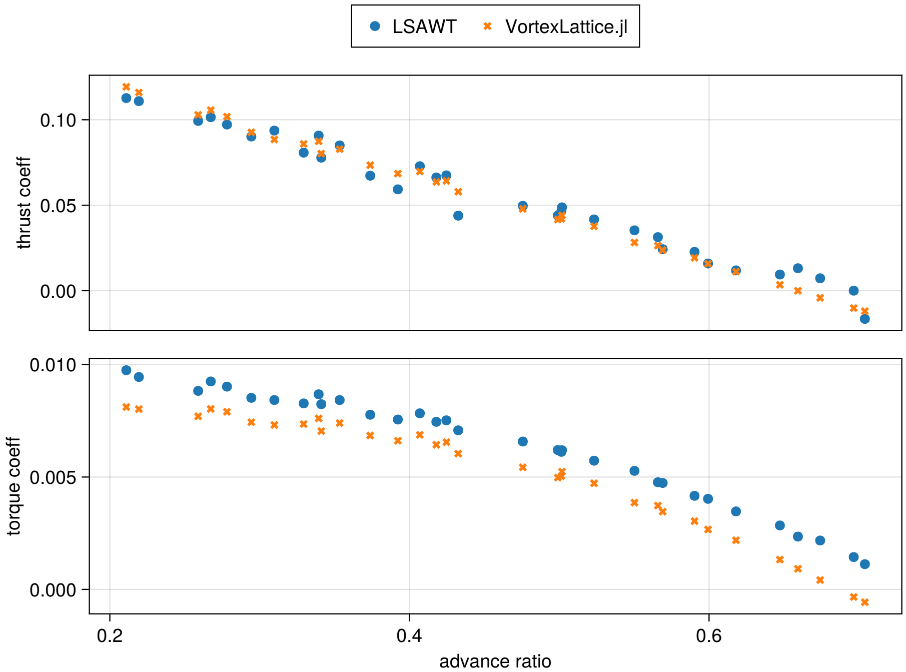

Fig. 1 Thrust and torque predictions from VortexLattice.jl compared to experimental data[14] acquired at NASA Langley's Low Speed Acoustic Wind Tunnel (LSAWT)

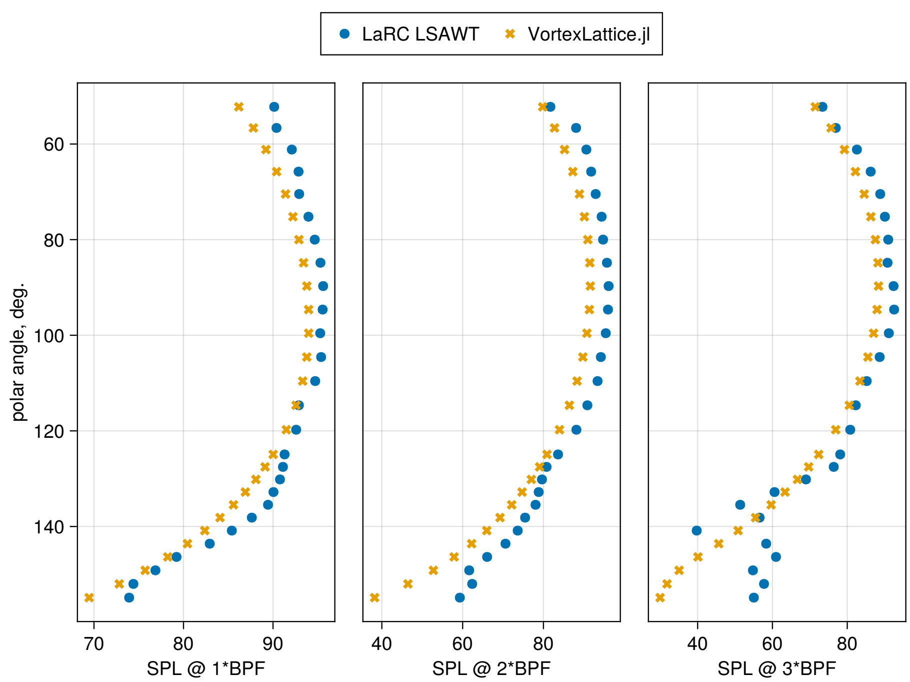

Fig. 2 Sound pressure level (SPL) predictions for the blade passing frequency ("1*BPF"), and two and three BPFs as a function of polar angle. Polar angles $< 90^\circ$ represent microphone locations upstream of the propeller rotation plane, $> 90^\circ$ downstream.

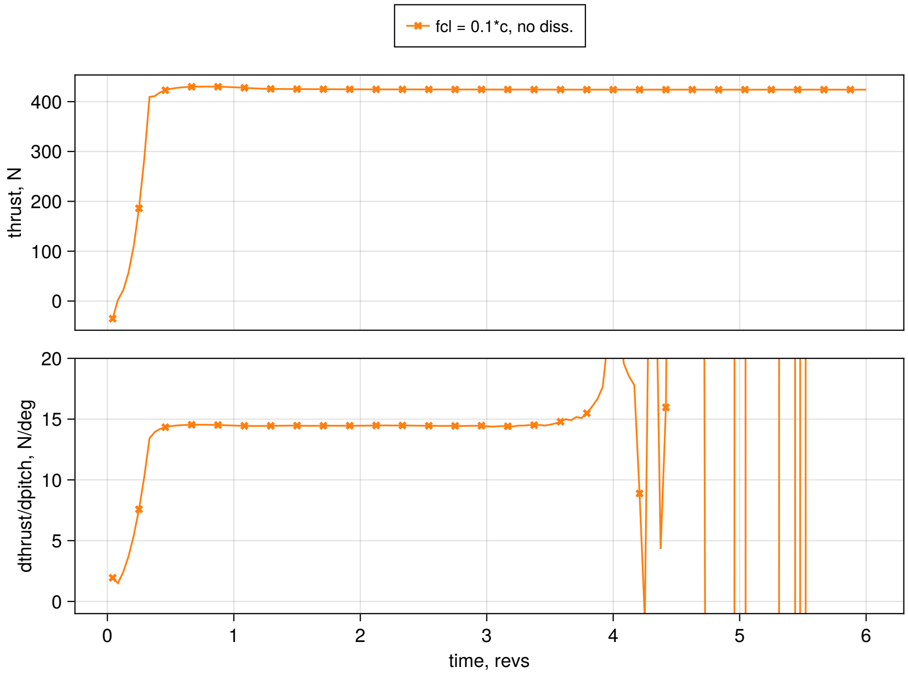

Fig. 3 Top plot: thrust prediction from the VLM as a function of time, where the time has been non-dimensionalized by the propeller rotation rate. Bottom plot: the derivative of thrust with respect to the blade pitch or collective angle, again displayed as a function of time. "fcl" is the finite core length used with the finite core model (see figure 5), and "no diss." indicates that no dissipation or dispersion are used with the wake vortex model (see equations 4–6).

90° downstream. Similar to the aerodynamic results in Figure 1, the acoustic levels are slightly underpredicted by the VortexLattice.jl+AcousticAnalogies.jl toolchain. Additionally, the compact F1A acoustic model in this work is only able to predict the tonal acoustics associated with the propeller blade—no broadband noise model is included, so of course any broadband noise sources will not be captured. Again, despite these limitations, we feel the level of accuracy shown in Figure 2 is adequate for preliminary design.

Figures 1 and 2 show the accuracy of the aerodynamic model when applied to a relevant propeller blade. To use gradient-based optimization methods in a design problem, however, we also need accurate, stable derivatives. We use ForwardDiff.jl, an automatic differentiation (AD) library, to calculate the derivatives of both the aerodynamic and acoustic models in this work, and verify the derivatives through comparisons with the finite difference method. Figure 3 shows the thrust predictions from the VLM as a function of time, and the derivative of the thrust with respect to the pitch (or collective) angle. We see that, after moving through transients associated with ramping the propeller rotation rate, the thrust coefficient assumes a nice, constant value. The derivative of the thrust coefficient also appears to achieve a steady value after moving past the transients until about three revolutions worth of time, after which it oscillates wildly. This behavior would obviously prevent successful gradient-based optimization.

Visualizing the VLM wake gives a possible clue to the distressing behavior of the derivatives in Figure 3. Figure 4 shows the VLM surface and wake panels for the run corresponding to Figure 3 at four revolutions worth of time after the start of the simulation, about one quarter revolution after the derivative instability becomes very apparent. We notice significant twisting of the wake elements in the downstream portion of the wake. We note that, in an unsteady VLM with a free wake, the motion of the wake is determined by the sum of the freestream velocity (constant in this work) and the velocity induced by each vortex associated with every surface and wake panel. This induced velocity is calculated via the Biot-Savart law, which, for a straight-line vortex segment, is

$$V = \frac{\Gamma}{4\pi} \left(\frac{\vec{r}_1 \times \vec{r}_2}{r_1 r_2 + \vec{r}_1 \cdot \vec{r}_2} \right) \left(\frac{1}{r_1} + \frac{1}{r_2} \right) \tag{3}$$

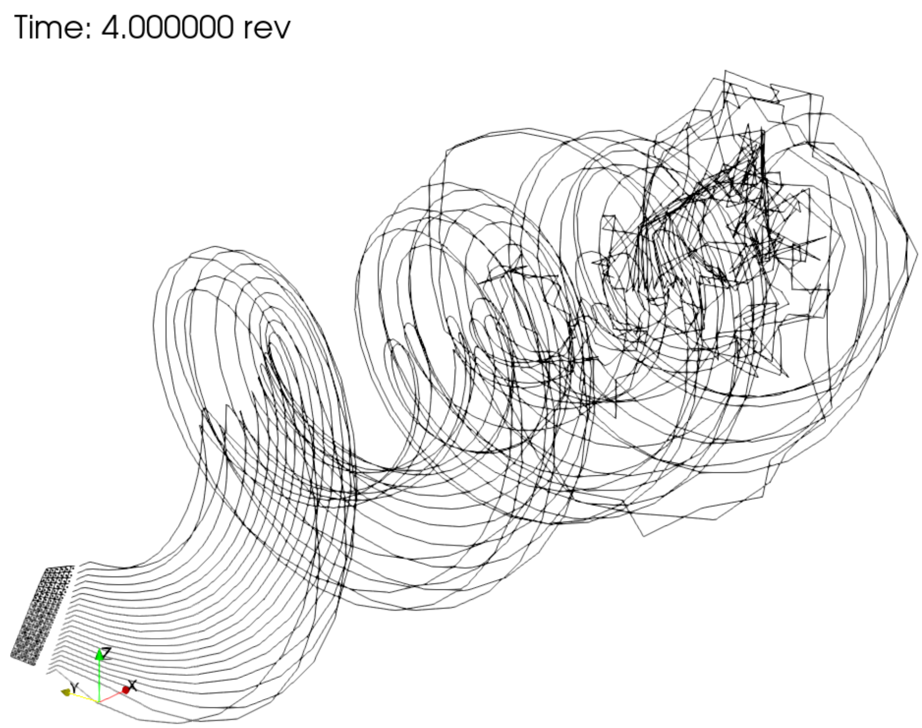

Fig. 4 Visualization of the VLM blade surface and wake elements for the run corresponding to Figure 3 at four revolutions

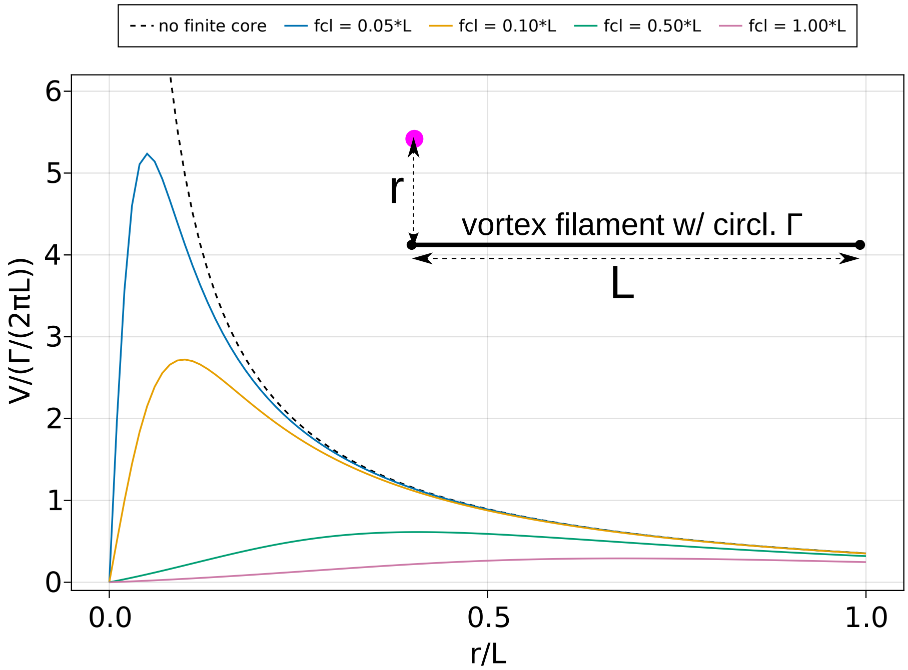

Fig. 5 Non-dimensionalized induced velocity as a function of distance from a straight-line vortex segment for various finite core lengths

where Γ is the vortex segment's circulation and $\vec{r}_1$ and $\vec{r}_2$ are the position vectors of the two endpoints of the vortex segment relative to the point where V is to be evaluated. As the distance between the evaluation point and the vortex segment is reduced the induced velocity increases sharply, and if the evaluation point lies on the vortex segment the induced velocity goes to infinity. To remedy this, many VLM codes use a finite core model, which modifies the Biot-Savart law to "smear out" the induced velocity near each vortex segment.

VortexLattice.jl's finite core model is depicted graphically in Figure 5, where the induced velocity is shown as a function of perpendicular distance from one of the segment's endpoints for various finite core length values. Without the finite core model the induced velocity clearly increases without bound as we move closer to vortex segment. With the finite core model enabled, however, the induced velocity goes to zero at the core of the vortex, and the region where the induced velocity is attenuated increases with increasing finite core length. We suggest that the twisting of the wake shown in Figure 4 and perhaps the instability of the thrust derivative shown in Figure 3 could be improved by increasing the finite core length. The impact of this change is studied next.

Figure 6 shows the significant effect the finite core length value has on the thrust coefficient and its derivative with respect to the blade pitch angle, and Figure 7 shows the impact of the same on the wake trajectory, where the twisting in the downstream portion of the wake is reduced. The orange curve in Figure 6 corresponds to the original results shown in Figure 3, where a small finite core length of $0.1c$ was used, with c being the chord length of the propeller blade, while the green curve uses a much larger finite core length of $1.0c$. Clearly increasing the finite core length stabilizes the thrust derivatives, but also has a strong effect on the value of the thrust itself. Figure 1 shows the thrust coefficient of the baseline propeller was relatively well predicted by VortexLattice.jl with the initial smaller finite core size of $0.1c$, so we suspect (and will soon confirm) that the larger finite core size results will negatively impact the comparison to the experimental data.

Figure 8 compares VortexLattice.jl's thrust and torque coefficients for the small and large finite core lengths to the same experimental data shown in Figure 1. Unfortunately, we indeed see that increasing the finite core length negativity impacts the accuracy of the aerodynamic predictions, especially for the lower advance ratios. The advance ratio is the distance the propeller moves forward during the time it takes to complete one revolution (in units of propeller diameters). For low advance ratios, the propeller wake will thus be closer to the blade than for higher advance ratios. This likely explains why increasing the finite core length has an especially deleterious effect on the low advance ratio cases: the

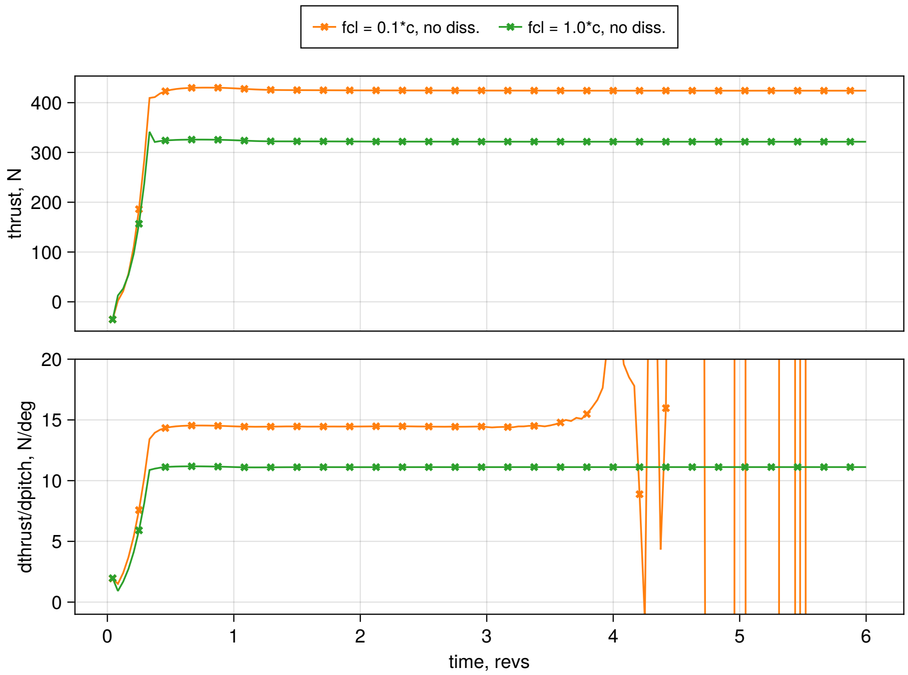

Fig. 6 Top plot: thrust coefficient predictions from the VLM as a function of time, where the time has been non-dimensionalized by the propeller rotation rate for a small ($0.1c$) and large ($1.0c$) finite core length value, where c is the chord length of the propeller blade. Bottom plot: the derivative of the thrust coefficient with respect to the blade pitch or collective angle, again displayed as a function of time for the same small and large finite core length values.

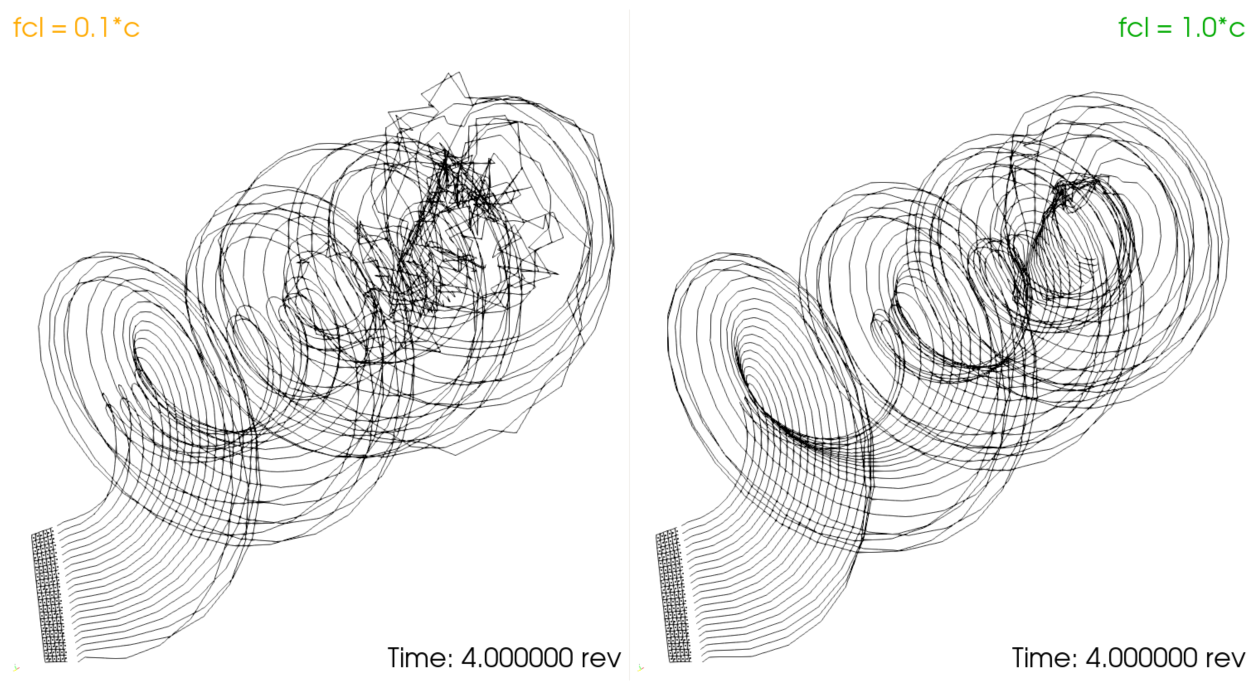

Fig. 7 Visualization of the VLM blade surface and wake elements for the run corresponding to Figure 6 for the small (left) and large (right) finite core lengths.

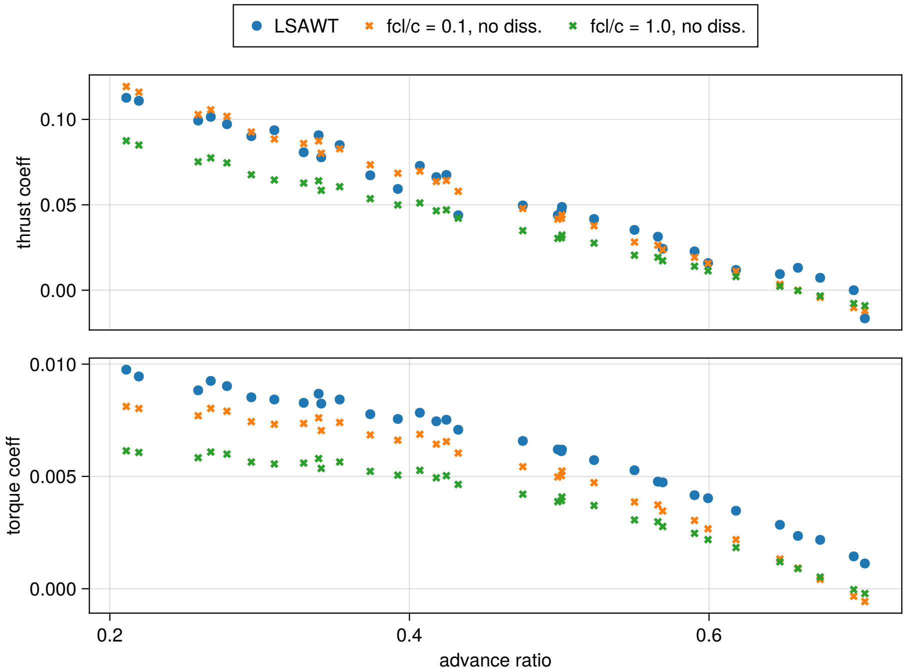

Fig. 8 Thrust and torque predictions from VortexLattice.jl compared to experimental data[14] acquired at NASA Langley's Low Speed Acoustic Wind Tunnel (LSAWT) for small and large finite core length sizes.

blade is in the finite core region of the upstream portion of the wake for these cases. On the other hand, the visualization of the wake in Figure 4 seems to suggest that the downstream portion of the wake is responsible for the derivative instability. We suspect (and will soon show) that using a small finite core length for wake elements near the blade, and a large finite core length for wake elements further downstream, would give us the best of both worlds: good agreement with experimental data *and* stable derivatives.

The previous VLM calculations use the same finite core width for all[‡] lifting surface (blade) and wake elements. This is consistent with the Kelvin circulation theorem, which states that the circulation of an ideal fluid will remain constant in time. Due to viscous effects, however, the circulation strength of a real propeller wake vortex will decrease with time, and the finite core size of each vortex will grow. This effect is typically captured in VLM implementations using semi-empirical vortex wake models. In this work, the wake vortex model described by Gregorio et al. [15] will be used. The model contains two components and three empirical parameters. The first component is the "vortex diffusion model" from Squire[16],

$$r_c = \sqrt{r_{c0}^2 + 4\alpha\delta\nu t} \tag{4}$$

where r_{c0} is the initial finite core length of a wake element (i.e., when the wake element is shed from the trailing edge of a lifting surface) and r_c is the finite core length at time t, where t is the age of the wake element. The Oseen coefficient α is an empirical parameter associated with the model, and $\delta\nu$ is an eddy viscosity defined by the relation

$$\delta\nu = \nu + a_1\Gamma \tag{5}$$

where ν is the kinematic viscosity, Γ is the circulation of the wake vortex element, and a_1 is the model's second empirical parameter. Taken together, equations 4 and 5 show how the finite core length grows with time, and how the rate of this growth is linked to the magnitude of a wake element's circulation Γ via a_1.

The second component of the wake vortex model is termed "vortex dissipation" and controls how the wake element's circulation changes with time:

$$\Gamma(t) = \Gamma_0 \exp\left(-\frac{bq}{s}t\right) \tag{6}$$

[‡]The finite core model is not enabled for surface-on-surface interactions involving the same lifting surface.

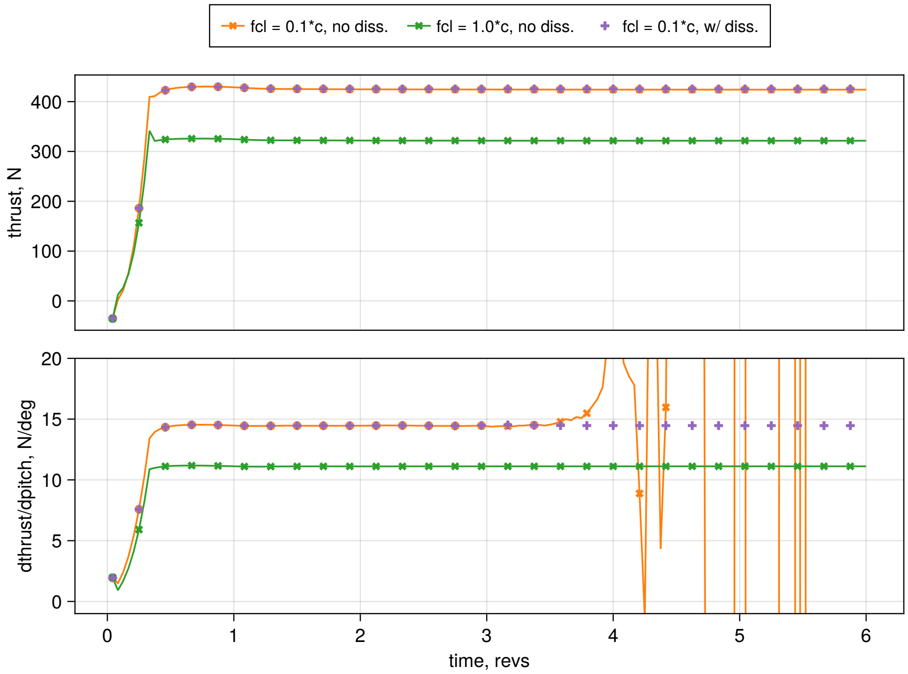

Fig. 9 Top plot: thrust coefficient predictions from the VLM as a function of time, where the time has been non-dimensionalized by the propeller rotation rate for a small $(0.1c)$ and large $(1.0c)$ constant finite core length value, and a small initial finite core length that grows with time. Bottom plot: the derivative of the thrust coefficient with respect to the blade pitch or collective angle, again displayed as a function of time for the same finite core lengths as the top plot.

where Γ_0 is the initial value of the vortex element's circulation (i.e., when it is shed by the blade trailing edge) and $\frac{bq}{s}$ is the third empirical parameter associated with the model. In this work, we set $\alpha = 1.25643$ and $\frac{bq}{s} = 2.5$, as suggested by Gregorio et al., but use $a_1 = 0$. Thus the finite core size of each wake element will grow with time, and each wake element's strength will decay with time, but the circulation strength of each wake element will not influence the finite core size growth. We have not completed a systematic study of the influence α, a_1, and $\frac{bq}{s}$ have on the accuracy of the VLM—instead, the values here are inspired by Gregorio et al., but with the ad hoc simplification of $a_1 = 0$. We emphasize that, as is shown in Gregorio et al., this vortex wake model was originally developed to better match particle image velocimetry (PIV) measurements of a rotor wake tip vortex, and not with any consideration of its effect on gradient-based optimization.

Figure 9 compares the results of using a $0.1c$ finite core length size combined with the dissipative and diffusive vortex wake model to the previous results (constant $0.1c$ and $1.0c$ finite core lengths). We see that using the dissipation model with a small initial finite core size has a similar stabilizing effect on the derivatives as does using a large, constant finite core size. The calculation with the small initial finite core size and dissipation model also appears to predict the same value for the thrust derivative as what found for the case with the small, constant finite core size, indicating that the former may better match experimental data. Figure 10 confirms this: the predictions with the vortex wake model and small initial finite core size are nearly identical to the predictions with the small constant finite core size.

III. Optimization Results

This section describes the results of two optimization cases using the tools described in Section II. The first case is an isolated propeller, and the second is a propeller upstream of a wing. The Mach 0.11 free stream, representative of a cruise condition, is aligned with the propeller rotation axis for both the isolated and propeller-wing configurations. The wing is four propeller blade radii long with a constant chord of one blade radius. The leading edge of the wing is

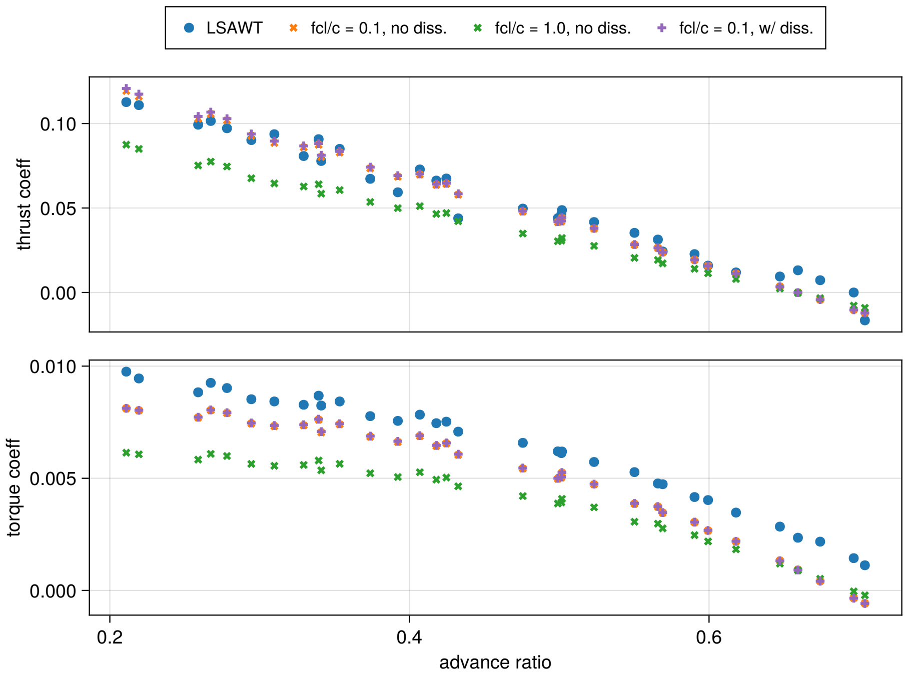

Fig. 10 Thrust and torque predictions from VortexLattice.jl compared to experimental data[14] acquired at NASA Langley's Low Speed Acoustic Wind Tunnel (LSAWT) for small and large constant finite core length sizes, and a small initial finite core size with a vortex dissipation model.

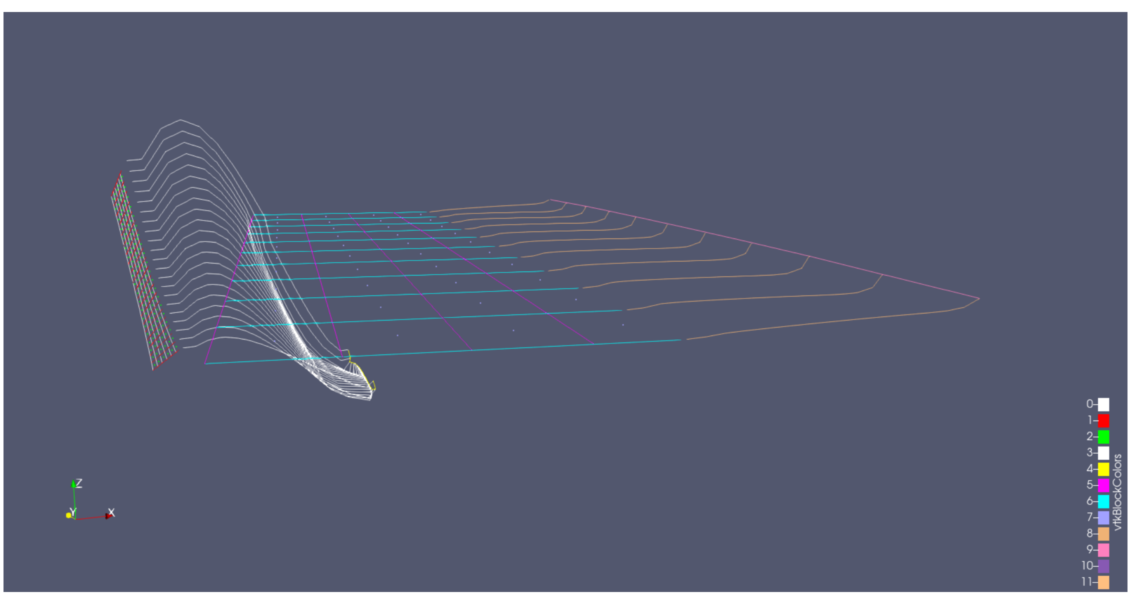

Fig. 11 View of the propeller-wing geometry. The freestream is aligned with the x-axis, i.e., moving from left to right. The blade and wing's wake elements are shown in white and brown, respectively.

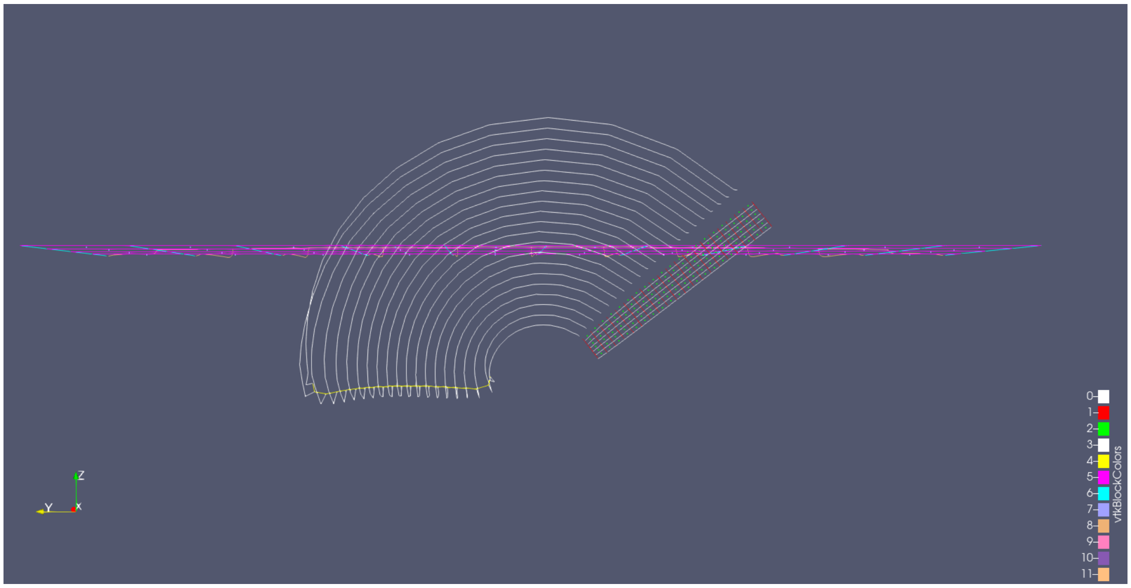

Fig. 12 View of the propeller-wing geometry. The freestream is aligned with the x-axis, i.e., moving into the page. The blade's wake elements are shown in white.

approximately $\frac{1}{4}$ of a blade radius behind the propeller trailing edge, and at a four degree angle of attack with respect to the free stream flow. The propeller rotation axis is at the wing mid-span plane, offset from the wing pitch change axis by a length of $\frac{1}{2}$ of a blade radii, below the pressure side of the wing. Figures 11 and 12 show the geometry of the (single) propeller blade and wing. We emphasize that the propeller-wing optimizations described in this work are meant to give the optimizer a more challenging problem to solve (through the unsteady loading the propeller blade experiences via its aerodynamic interaction with the wing). As will be seen, none of the design variables will affect the wing's geometry or position relative to the propeller blade.

The configuration of the two optimization cases (again, isolated propeller and propeller-wing) are identical, and are summarized in Table 2. The goal is to maximize the propulsive efficiency of the propeller subject to a thrust and noise constraint. The design variables include the chord distribution (defined by cubic B-splines with six control points, provided by the BSplineKit.jl[17] software package), the collective (pitch) angle, and the propeller rotation rate. For each of the two cases, the optimization is first run without a noise constraint, and the sideline overall sound pressure level (OASPL) value is recorded. The value of the noise constraint is then progressively reduced relative to that value to

	Variable	Lower Bound	Upper Bound	Count
maximize	propeller efficiency			
with respect to	chord distribution spline control points	0.5 in.	9.0 in.	6
	collective (pitch) angle	$-10°$	$85°$	1
	RPM	2000 rev/min	9000 rev/min	1
subject to	thrust	90.7 N	90.7 N	1
	downstream OASPL	x	x	1
	maximum chord concavity (optional)	$-\infty$	0	1

Table 2 Parameters for the propeller optimization problem. The downstream OASPL constraint value is swept to capture the influence of the noise constraint on the blade design. The optimizations are attempted with and without the chord concavity constraint.

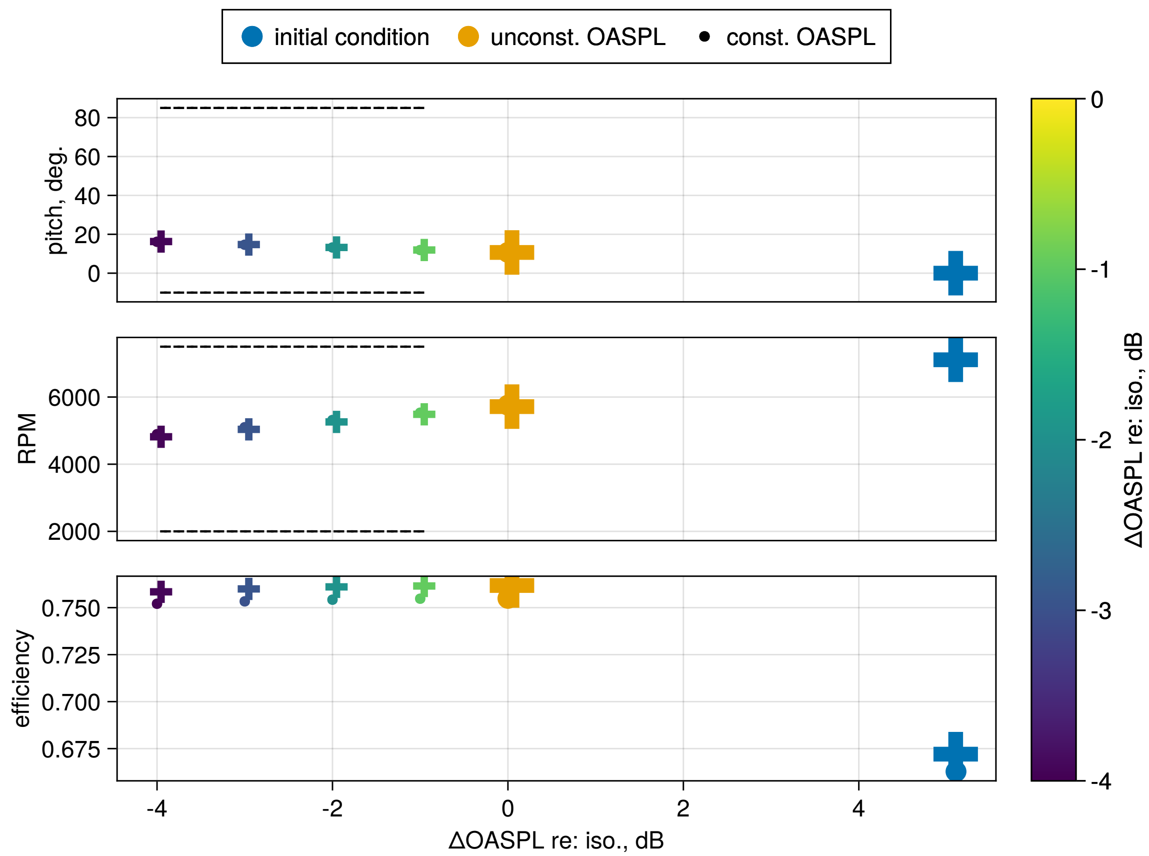

Fig. 13 Collective (pitch) angle and RPM design variables and the efficiency objective as a function of the value of the OASPL noise constraint for optimizations including the chord concavity constraint. Circles indicate the isolated propeller, which usually overlap the crosses for the propeller-wing. Blue markers are for the baseline propeller design, orange the optimizations without an acoustic constraint, and the colormaped symbols include the acoustic constraint. The dashed black lines indicate lower and upper design variable limits.

capture the effect of the noise constraint on the design variables and propeller efficiency objective. A chord concavity constraint $\frac{d^2c}{dr^2} \leq 0$, where c is the chord and r the radial position along the blade, was imposed to force the optimizer to produce reasonable-looking designs. Optimization results will be shown with and without the chord concavity constraint.

We use the SNOPT optimizer[18] to solve the optimization problem described in Table 2. Derivatives of the efficiency objective function and each constraint are calculated by the ForwardDiff.jl[19] software package and provided to SNOPT to aid convergence. The SNOPT optimizer is called through the SNOW.jl[§] software package.

The results of the optimizations described by Table 2 are shown in Figures 13 and 14 for the optimizations including the chord concavity constraint. SNOPT was able to successfully converge each optimization (for those familiar with SNOPT, all optimizations achieved a "`0/1`" exit status). Figure 13 shows that the optimizer decides to significantly increase the collective or pitch angle and decrease the RPM for the run without the noise constraint. This allows the optimizer to increase the propeller efficiency by slowing down the propeller blade while still satisfying the thrust constraint. As the noise constraint is tightened, the optimizer continues to increase the collective and decrease the RPM. This comes with a slight efficiency penalty. We note there is little difference between the isolated propeller and propeller-wing results.

Figure 14 shows the effect varying the OASPL constraint has on the chord distribution for both the isolated propeller

[§]`https://github.com/byuflowlab/SNOW.jl`

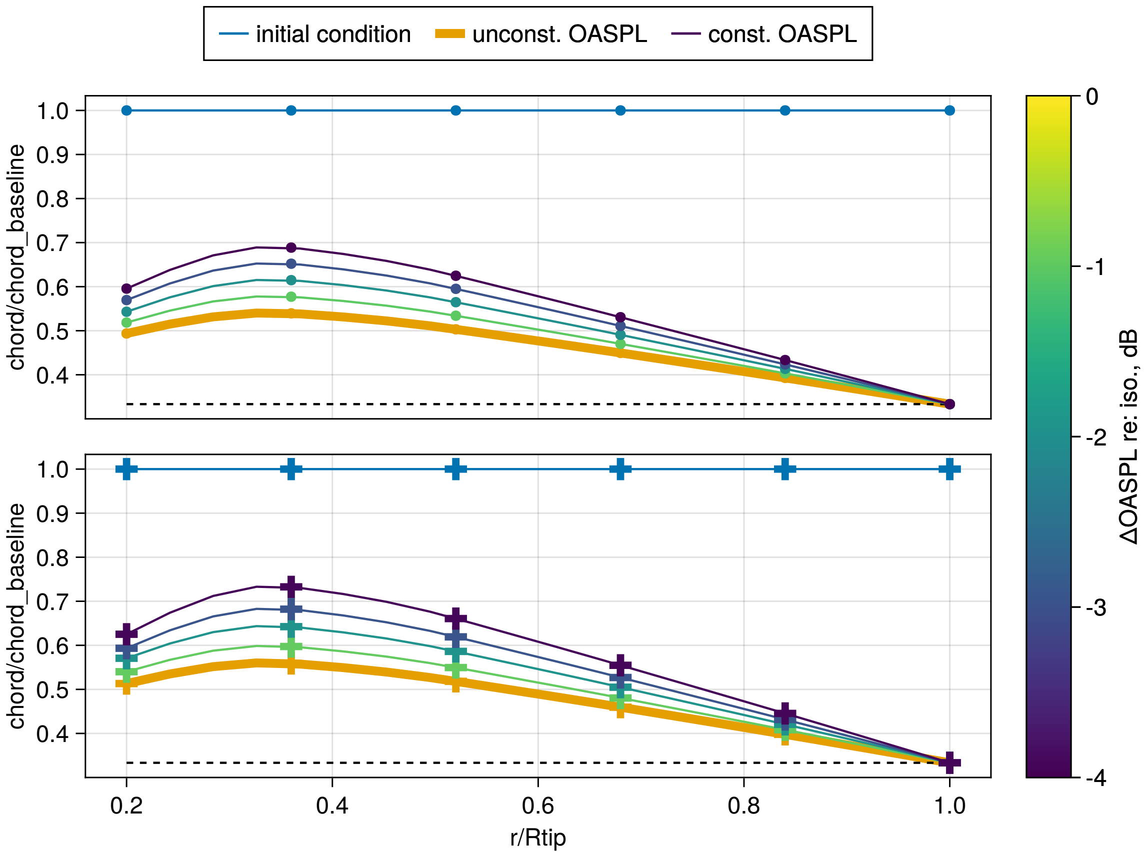

Fig. 14 Chord distribution for the isolated (top, circular markers) and propeller-wing (bottom, cross markers) optimizations along the blade span for optimizations including the chord concavity constraint. The blue and orange curves indicate the baseline design and design without an acoustic constraint, respectively. The color bar indicates the value of the OASPL constraint for the acoustically-constrained optimizations (the x-axis of Figure 13). The dashed black lines indicate the lower limit on the chord control point design variables.

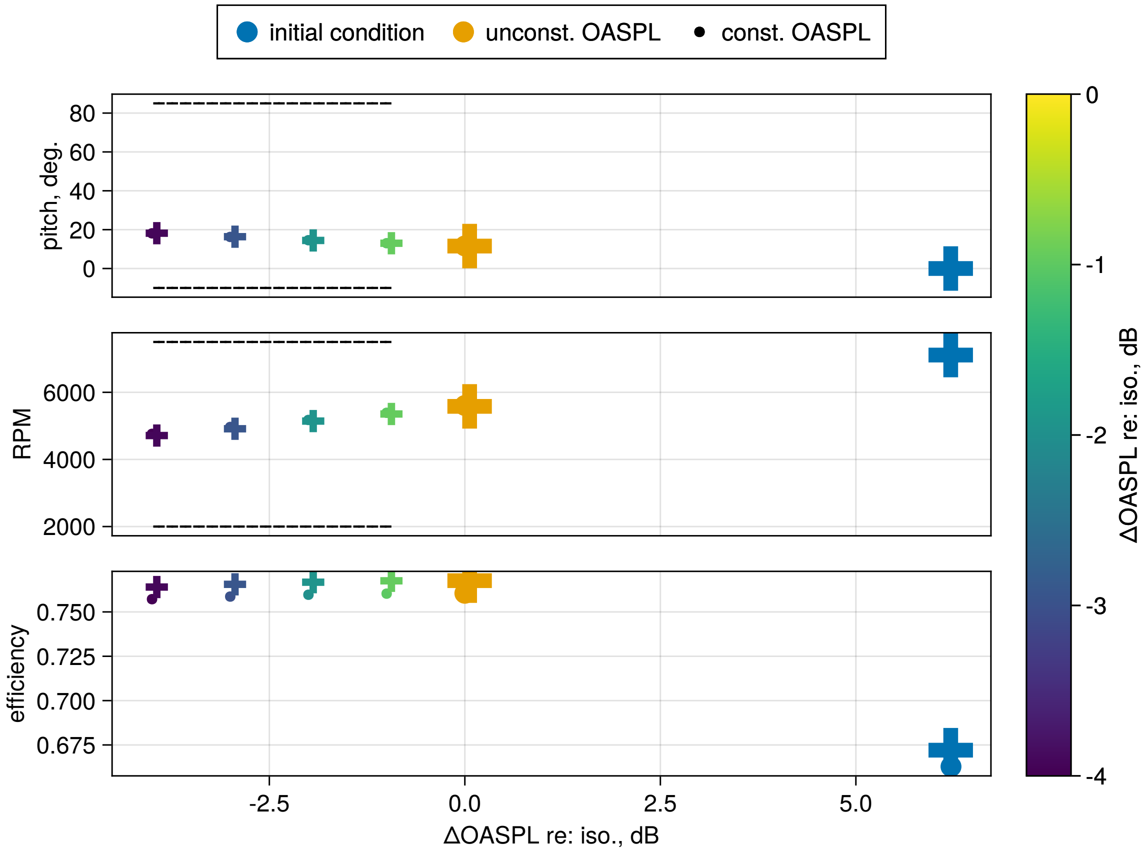

Fig. 15 Collective (pitch) angle and RPM design variables and the efficiency objective as a function of the value of the OASPL noise constraint for optimizations without the chord concavity constraint. Circles indicate the isolated propeller, crosses the propeller-wing. Blue markers are for the baseline propeller design, orange the optimizations without an acoustic constraint, and the viridis-colored include the acoustic constraint. The dashed black lines indicate lower and upper design variable limits.

and propeller-wing configurations, all including the chord concavity constraint. For all cases, the optimizer decides to minimize the chord at the tip, to reduce both tip losses and the thickness noise associated with the fastest-moving part of the blade. As the OASPL constraint is tightened, the optimizer steadily increases the chord throughout the blade, allowing the blade to maintain the required thrust at the lower RPM value. We note that each chord distribution is at the upper limit of the chord concavity constraint, as the chord is linear for approximately the outer third of the blade, and thus has a second derivative with respect to radial position of zero. Again, little difference between the isolated propeller and propeller-wing results is observed.

The results of the optimizations described by Table 2 without the chord concavity constraint are shown in Figures 15 and 16 for the optimizations including the chord concavity constraint. Again, SNOPT was able to successfully converge each optimization. The pitch, RPM, and efficiency behavior with respect to the noise constraint is quite similar to the results including the chord concavity constraint (Figure 13). Much more significant differences are seen in the chord distribution results. Figure 16 shows that for both configurations (isolated propeller and propeller-wing), the optimizer decided to set the two outboard chord control points to the lower limit. This should, of course, minimize tip losses, and may indicate that the diameter of the propeller blade is larger than necessary. The oscillations in the chord distribution are not representative of actual propeller designs, and point to a weakness in the present model, and warrant further study.

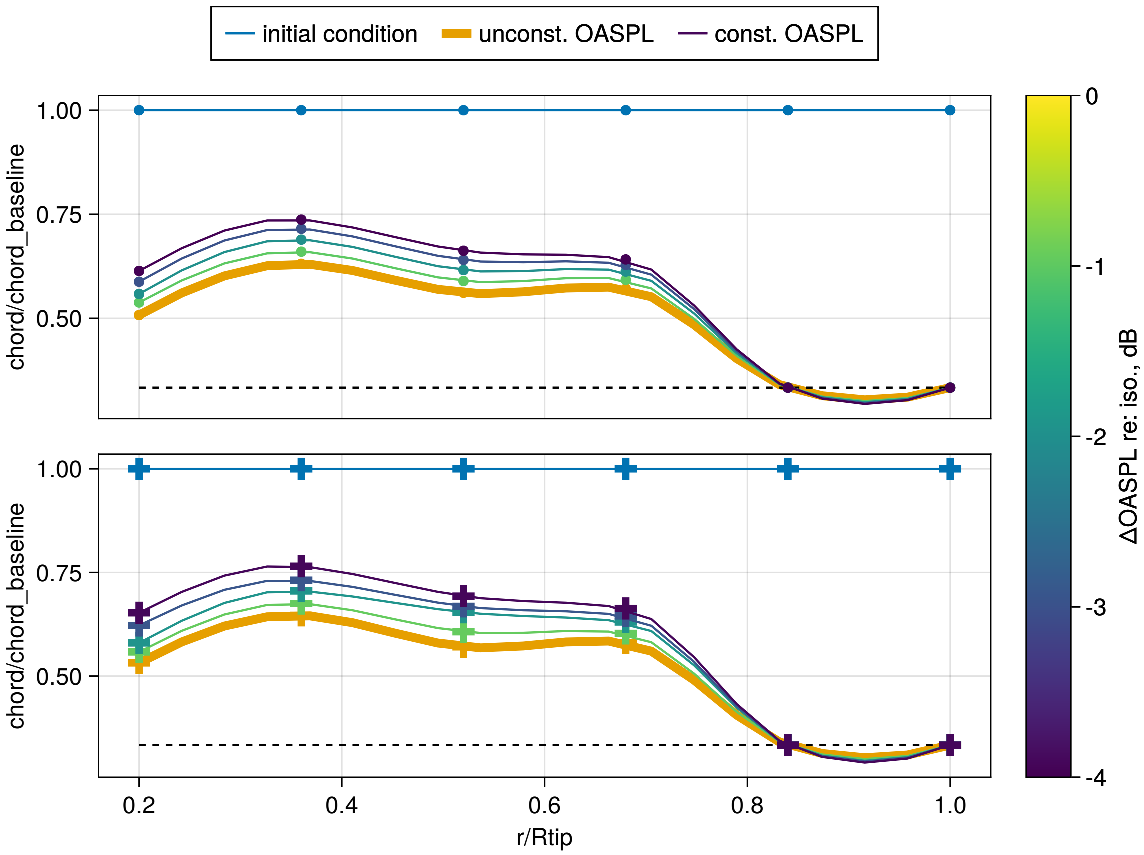

Fig. 16 Chord distribution for the isolated (top, circular markers) and propeller-wing (bottom, cross markers) optimizations along the blade span for optimizations without the chord concavity constraint. The blue and orange curves indicate the baseline design and design without an acoustic constraint, respectively. The color bar indicates the value of the OASPL constraint for the acoustically-constrained optimizations (the x-axis of Figure 15). The dashed black lines indicate the lower limit on the chord control point design variables.

IV. Conclusions

In this work, aerodynamic-acoustic optimizations of an isolate propeller and propeller-wing system at a cruise condition were performed. The aerodynamic model of the propeller was provided by an implementation of the unsteady vortex lattice method, and the tonal acoustics were modeled using the compact form of Farassat's formulation 1A. A vortex wake model was shown to stabilize the derivatives of the VLM without sacrificing the accuracy of the method. This model increases the finite core length and decreases the circulation strength associated with each wake element as the wake convects downstream. The value of the empirical parameters associated with the vortex wake model were influenced by Gregorio et al. [15], but did not include coupling between the instantaneous wake vortex strength and finite core size growth rate. The effect of this coupling and the influence of the other empirical parameters will be studied in the future.

The results of this work showed little difference between the optimized isolated propeller and propeller-wing designs. While each optimization attempted was successfully converged, a chord concavity constraint was required to coax the optimizer to produce realistic-looking chord distributions. The reason for this is not understood at present, and will be studied in the future.

Overall, this work shows that it is possible to use a free wake vortex lattice method and Farassat's formulation 1A to perform gradient-based aerodynamic-acoustic optimizations, provided a reasonable wake vortex model is used to stabilize the derivatives of the VLM. In the future, we would like to increase the complexity of the optimization cases, e.g., by adding sweep as a design variable, attempting multi-point optimizations that include the hover condition, or by adding a broadband noise model to complement the tonal acoustic predictions provided by F1A. Ultimately we hope these tools will eventually be useful for computationally efficient urban air mobility and advanced air mobility design tasks.

Acknowledgments

We thank Nikolas Zawodny and Leonard Lopes of NASA Langley Research Center for the LSAWT experimental data shown in Figures 1 and 2, and Christopher J. Miller of NASA Glenn Research Center for numerous helpful discussions and reviewing an early form of this paper. We thank Taylor McDonnell and Andrew Ning of Brigham Young University for VortexLattice.jl. We thank NASA's Transformational Tools and Technologies (TTT) project for funding this work.

References

[1] Rizzi, S. A., Huff, D. L., Boyd, D. D., Jr., Bent, P., Henderson, B. S., Pascioni, K. A., Sargent, D. C., Josephson, D. L., Marson, M., He, H. B., and Snider, R., "Urban Air Mobility Noise: Current Practice, Gaps, and Recommendations," Tech. Rep. NASA/TP-2020-5007433, NASA Langley Research Center, Hampton, VA, United States, October 2020.

[2] Içke, R. Ö., Baysal, O., Lopes, L. V., and Diskin, B., "Optimizing Proprotor Blades Using Coupled Aeroacoustic and Aerodynamic Sensitivities," *AIAA AVIATION 2021 FORUM*, American Institute of Aeronautics and Astronautics, 2021. https://doi.org/10.2514/6.2021-3037, URL http://dx.doi.org/10.2514/6.2021-3037.

[3] Ingraham, D., Gray, J. S., and Lopes, L. V., "Gradient-Based Propeller Optimization with Acoustic Constraints," *AIAA Scitech 2019 Forum*, American Institute of Aeronautics and Astronautics, 2019. https://doi.org/10.2514/6.2019-1219.

[4] Katz, J., and Plotkin, A., *Low-speed aerodynamics*, 2nd ed., Cambridge university press, 2001.

[5] Drela, M., *Flight vehicle aerodynamics*, The MIT Press, Cambridge, Massachusetts, 2014.

[6] Chang, L. K., and Sullivan, J. P., "Optimization of Propeller Blade Twist by an Analytical Method," *AIAA Journal*, Vol. 22, No. 2, 1984, p. 252–255. https://doi.org/10.2514/3.48441, URL http://dx.doi.org/10.2514/3.48441.

[7] Miller, C. J., "Optimally Designed Propellers Constrained By Noise," Ph.D. thesis, Purdue University, 1984.

[8] Cho, J., and Lee, S.-c., "Propeller blade shape optimization for efficiency improvement," *Computers and Fluids*, Vol. 27, No. 3, 1998, p. 407–419. https://doi.org/10.1016/s0045-7930(97)00035-2, URL http://dx.doi.org/10.1016/S0045-7930(97)00035-2.

[9] Burger, C., Hartfield, R., and Burkhalter, J., "Propeller Performance Optimization Using Vortex Lattice Theory and a Genetic Algorithm," *44th AIAA Aerospace Sciences Meeting and Exhibit*, 2006. https://doi.org/10.2514/6.2006-1067, URL http://dx.doi.org/10.2514/6.2006-1067.

[10] Burger, C., Hartfield, R., and Burkhalter, J., "Performance and Noise Optimization of a Propeller using the Vortex Lattice Method and a Genetic Algorithm," *48th AIAA/ASME/ASCE/AHS/ASC Structures, Structural Dynamics, and Materials Conference*, American Institute of Aeronautics and Astronautics, 2007. https://doi.org/10.2514/6.2007-1883, URL http://dx.doi.org/10.2514/6.2007-1883.

[11] Farassat, F., "Linear Acoustic Formulas for Calculation of Rotating Blade Noise," *AIAA Journal*, Vol. 19, No. 9, 1981, pp. 1122–1130. https://doi.org/10.2514/3.60051.

[12] Farassat, F., "Derivation of Formulations 1 and 1A of Farassat," Tech. Rep. NASA/TM 2007-214853, NASA Langley Research Center, Hampton, VA, United States, Mar 2007.

[13] Lopes, L. V., "Compact Assumption Applied to Monopole Term of Farassat's Formulations," *Journal of Aircraft*, Vol. 54, No. 5, 2017, p. 1649–1663. https://doi.org/10.2514/1.c034048.

[14] Zawodny, N., and Lopes, L. V., personal communication, 2021.

[15] De Gregorio, F., Visingardi, A., and Iuso, G., "An Experimental-Numerical Investigation of the Wake Structure of a Hovering Rotor by PIV Combined with a Γ2 Vortex Detection Criterion," *Energies*, Vol. 14, No. 9, 2021, p. 2613. https://doi.org/10.3390/en14092613, URL http://dx.doi.org/10.3390/en14092613.

[16] Squire, H. B., "The Growth of a Vortex in Turbulent Flow," *Aeronautical Quarterly*, Vol. 16, No. 3, 1965, p. 302–306. https://doi.org/10.1017/s0001925900003516, URL http://dx.doi.org/10.1017/S0001925900003516.

[17] Polanco, J. I., "BSplineKit.jl: a collection of B-spline tools in Julia," , July 2021. https://doi.org/10.5281/zenodo.7272999, URL https://doi.org/10.5281/zenodo.7272999.

[18] Gill, P., Murray, W., and Saunders, M., "SNOPT: An SQP Algorithm for Large-Scale Constrained Optimization," *SIAM Review*, Vol. 47, No. 1, 2005, pp. 99–131. https://doi.org/10.1137/S0036144504446096.

[19] Revels, J., Lubin, M., and Papamarkou, T., "Forward-Mode Automatic Differentiation in Julia," *arXiv:1607.07892 [cs.MS]*, 2016. URL https://arxiv.org/abs/1607.07892.